

# A Canonical Experiment Comparing Tomographic and Plenoptic PIV

Eric A. Deem,<sup>1,\*</sup> Dominic Agentis,<sup>1</sup> Francois Nicolas,<sup>1</sup> Louis N. Cattafesta,<sup>1</sup>  
Timothy Fahringer,<sup>2</sup> Brian Thurow<sup>2</sup>

<sup>1</sup>Florida Center for Advanced Aero-Propulsion, Florida State University, Tallahassee, Florida, USA

<sup>2</sup>Advanced Flow Diagnostics Laboratory, Auburn University, Auburn, Alabama, USA

\*corresponding author: edeem@fsu.edu

---

**Abstract** Instantaneous volumetric measurements of flow velocity are invaluable. Plenoptic PIV represents the latest state of the art in non-intrusive, volumetric velocity measurement technology. A comparable method is Tomographic PIV. Although Tomographic PIV provides reliable quantitative results, this technique has limitations due to the cumbersome nature of using multiple cameras. Plenoptic PIV does not suffer from this drawback. This technique employs the concept of light field photography using the plenoptic camera [10] [13]. This work evaluates the current performance of Plenoptic PIV by providing a quantitative comparison of data acquired using Plenoptic PIV, Tomographic PIV and Stereoscopic PIV. The PIV data were acquired in the wake of a finite cylinder protruding through a boundary layer at  $Re_d = 38,000$  with  $\delta/h = 0.45$  and  $h/d = 3$ . This platform provides a canonical three-dimensional flow field that contains several interesting features of varying scale and complexity. Stereo PIV measurements are also provided as a comparison. In preparing this quantitative comparison, methods regarding the plenoptic volume reconstruction scaling are discussed, plenoptic image processing concerns are addressed, and Plenoptic PIV vector statistical quantities are analyzed. Although this technique is still in its infancy, Plenoptic PIV measurements compare favorably to the other measurements.

**Keywords:** Plenoptic, Tomographic, PIV, Cylinder, Wake

---

## 1 Introduction

Turbulent flows are inherently three-dimensional, therefore the ability to visualize a 3-D snapshot of turbulent flow is extremely valuable to fluid dynamicists. Additionally, interesting fluid dynamics can be buried in secondary flows that may not be observed by point or planar measurement methods. The state of the art method in producing 3-D velocity snapshots in experimental flow settings is Plenoptic Particle Image Velocimetry (PIV). Plenoptic PIV is an evolution of conventional PIV in which a plenoptic camera is employed. With the advent of the plenoptic camera, it is possible to sample a snapshot of a light field with a single device. The light field is defined as the total distribution of light within some space [10]. Having a full description of the light field allows for a leap in digital imaging capabilities, including: digital refocusing, digital perspective change, extended depth of field, and volumetric light-source reconstruction.

Another technology used to acquire volumetric velocity measurements is Tomographic PIV. Tomographic PIV was first introduced in the literature by Elsinga et al. [3]. Like Plenoptic PIV, this method provides an instantaneous, non-intrusive measurement of a volume of flow. Within the past decade, Tomographic PIV has been applied to various experimental fluid dynamic platforms. Operational considerations are compiled in the text by Scarano [18].

In Tomographic PIV, the light field is recorded from multiple (typically 4) conventional cameras with significantly different viewing angles of the measurement region. Unfortunately, many flow facilities do not have the required optical access for Tomographic PIV.

Since only one optical perspective is required for Plenoptic PIV, acquiring volumetric flow data in cases with limited optical access is now a possibility. Of course, some trade-offs exist. In plenoptic photography, individual pixels are being used to store the angular information of the light field entering the camera. In other words, planar spatial information is traded for angular information. Thus, an increase in the number of pixels is required to offset the decrease in planar resolution.

This work is designed to compare Plenoptic PIV and Tomographic PIV measurements in order to highlight their respective strengths and weaknesses. Using both Plenoptic and Tomographic PIV, instantaneous velocity information is obtained in a volume within the wake of a small cylinder protruding from a boundary layer. These results are compared side by side, along with Stereoscopic PIV (SPIV) data as a metric. The following sub-sections are intended to provide the reader with a brief introduction to the plenoptic PIV concept.

## 1.1 The Plenoptic Camera

With conventional digital photography, individual pixels record relative brightness levels from incident rays. However, no information regarding the incoming trajectory of the light is retained. In contrast, the plenoptic camera samples the spatial distribution of light in addition to information regarding the trajectory (angle) of the incoming light. This information can be used to form a representation of the light field within the camera's field of view.

The plenoptic camera retains the angular information by the inclusion of a microlens array mounted between the main lens of the camera and the photosensor. This microlens array is the only design difference between a plenoptic camera and a conventional digital camera. The plenoptic camera prototype design is described in Lynch et al. [11]. However, the plenoptic camera used in this endeavor is part of the second generation of plenoptic PIV cameras developed at the Advanced Flow Diagnostics Laboratory (AFDL) at Auburn University. In contrast to the prototype, this camera contains a higher number of more densely packed microlenses and twice the number of pixels. The next section describes how the light field is coded onto the plenoptic camera photosensor.

## 1.2 The Plenoptic Image

To provide the reader with a fundamental understanding of the plenoptic camera, 2-D ray tracing diagrams will be used. Figure 1 shows 2-D ray tracing diagrams for both a conventional camera and the plenoptic camera. For both diagrams, the main lens has a focal length of  $f_M$ . The only difference between the two diagrams in Figure 1 is the addition of the array of smaller lenses for the plenoptic camera diagram. This linear array of lenses is a simplified representation of the microlens array used in the actual plenoptic camera. The microlens focal length is  $f_\mu$ .

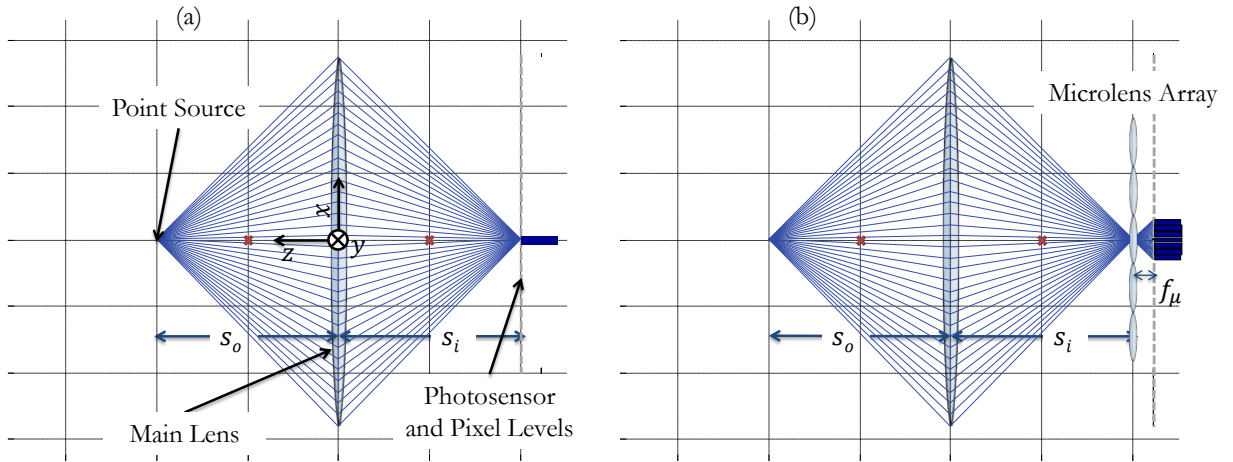


Fig. 1 2-D ray-tracing diagram illustrating the rays within a simplified (a) conventional camera and a (b) plenoptic camera from a point source of light. The main lens focal distance is denoted by the red cross. The ray tracing coordinate system is shown.

In Figure 2, a single ray is highlighted on the plenoptic camera ray tracing diagram. The position and angular offset of the ray is labeled to illustrate the refraction of the ray within the plenoptic camera. With knowledge of the initial position and trajectory of the ray  $(x_1, \theta_1)$ , ray transfer matrices can be used to calculate the location that the ray intersects the photosensor  $(x_4)$ . In order to orient the reader, the matrix describing the propagation of the light ray along some distance  $d$  is  $T_d = [1, 0; d, 1]$ , and the matrix describing the refraction through a lens of some focal length,  $F$  is  $R_F = [1, -1/F; 0, 1]$ . The path of the light ray from its origin through the main lens to the microlens array is described by  $[\theta_2, x_3]^T = (T_{s_i} R_{f_M} T_{s_o}) [\theta_1, x_1]^T$

At the microlens array, the x-coordinate must be shifted relative to the current microlens optical axis. This is referred to in prior literature as "affine optics" [8]. Assuming that the x-locations of all of the microlenses are known, the relative x-coordinate is defined as  $x'_3 = x_3 - x_\mu$ . The variable  $x_\mu$  is the central

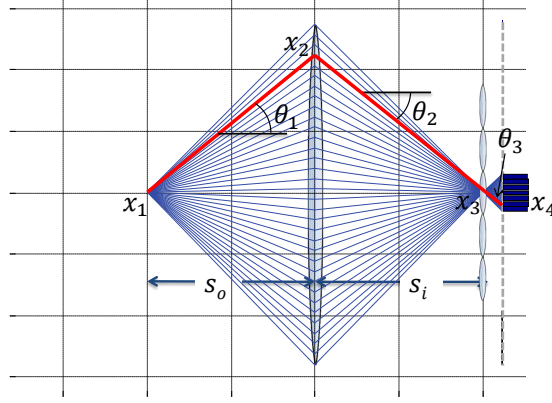


Fig. 2 Position and angular offset for an arbitrary ray to illustrate the refraction of the ray within the plenoptic camera. The angles and positions used for ray tracing are labeled.

position of the current microlens. Then, the refraction of the ray at the current microlens is described by:  $[\theta_3, x'_3]^T = R_{f_\mu} [\theta_2, x_3]^T$ .

Finally, the translation of the ray from the microlens array to the photosensor is described by:  $[\theta_3, x_4]^T = T_{f_\mu} [\theta_3, x_3]^T$ .

Based on these relations, the light field can be traced back through the camera from a plenoptic image. It is assumed that the experimentalist has full knowledge of the location of each microlens with respect to the photosensor. This is accomplished by a calibration step before plenoptic image processing can take place. The calibration process used in this study is described in [5].

For the point source illustrated in Figure 1, consider an arbitrary pixel at  $x_4$ . The corresponding microlens position is known, therefore a range of  $\theta_3$  can be calculated that contains all possible angles that the incident light rays could have subtended.

$$\theta_{3,max} = \tan^{-1} \left( \frac{d_\mu/2 - x_4}{f_\mu} \right), \quad \theta_{3,min} = \tan^{-1} \left( \frac{-d_\mu/2 - x_4}{f_\mu} \right). \quad (1)$$

The parameter  $d_\mu$  is the diameter of the microlens. Since  $x_4$  and the range of  $\theta_3$  is known for this pixel, the range of light rays that resulted in that image can be traced back to the source by inverting the matrices used to form the plenoptic image.

$$\begin{bmatrix} \theta_{3,max} \\ x_{3,max} \end{bmatrix} = T_{f_\mu}^{-1} \begin{bmatrix} \theta_{3,max} \\ x_4 \end{bmatrix}, \quad \begin{bmatrix} \theta_{2,min} \\ x'_{3,max} \end{bmatrix} = R_{f_\mu}^{-1} \begin{bmatrix} \theta_{3,max} \\ x'_{3,max} \end{bmatrix}, \quad \begin{bmatrix} \theta_{1,min} \\ x_{1,max} \end{bmatrix} = T_{s_o}^{-1} R_{f_M}^{-1} T_{s_i}^{-1} \begin{bmatrix} \theta_{2,min} \\ x_{3,max} \end{bmatrix} \quad (2)$$

$$\begin{bmatrix} \theta_{3,min} \\ x_{3,min} \end{bmatrix} = T_{f_\mu}^{-1} \begin{bmatrix} \theta_{3,min} \\ x_4 \end{bmatrix}, \quad \begin{bmatrix} \theta_{2,max} \\ x'_{3,min} \end{bmatrix} = R_{f_\mu}^{-1} \begin{bmatrix} \theta_{3,min} \\ x'_{3,min} \end{bmatrix}, \quad \begin{bmatrix} \theta_{1,max} \\ x_{1,min} \end{bmatrix} = T_{s_o}^{-1} R_{f_M}^{-1} T_{s_i}^{-1} \begin{bmatrix} \theta_{2,max} \\ x_{3,min} \end{bmatrix} \quad (3)$$

This yields a point and slope for the lines that define the envelope of all possible rays that could have resulted in the pixel signal at  $x_4$ . For simplicity, it has been assumed that the pixel is infinitesimal. This is illustrated in Figure 3.

Repeating this process for every illuminated pixel on a plenoptic image results in a discrete representation of the light field. A 2-D sketch of the light field sampled from a point source is shown in Figure 4. This manner for representing the lightfield lends itself well to illustrating how the light can be traced back through the plenoptic camera.

In PIV, the observed displacement of seed particles is used to calculate velocity vectors in the flow field. Therefore, it is not sufficient to have a representation of the light field - the 3-D distribution of the light sources responsible for generating the light field must be known. The following subsection describes the manner in which light sources are reconstructed from the measured light field.

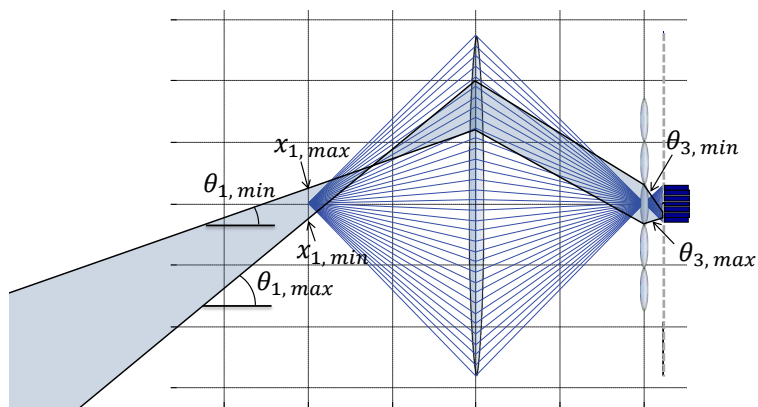


Fig. 3 The brightness of an arbitrary pixel traced back through the plenoptic camera.

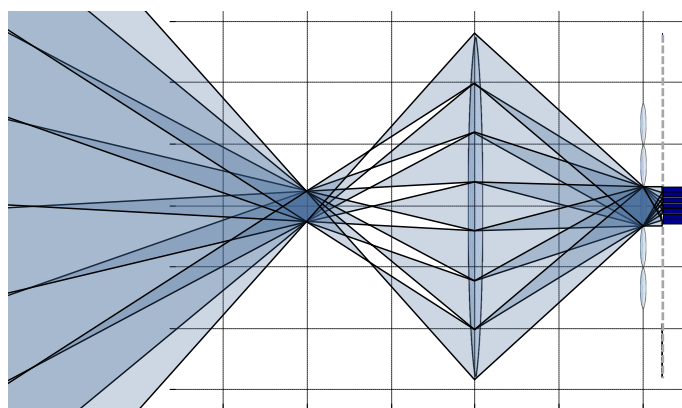


Fig. 4 The back projection of the light field from the signal recorded on the photosensor.

## 2 Particle Volume Reconstruction

Both Plenoptic and Tomographic PIV require some processing of the raw images in order to represent the 3-D particle distribution. Similar to how a digital photograph is composed of discrete pixels, the reconstructed volumes for Plenoptic and Tomographic PIV must be built by discrete elements to be manipulated digitally. These discrete volume elements are referred to as “voxels” (volumetric pixels). In reconstructing the light sources within a volume, each voxel is assigned a value corresponding to the intensity of light generated (or scattered) at that point in space.

To reconstruct a volume suitable for PIV from plenoptic images, a process known as filtered refocusing is applied. Briefly, this method is based on the conventional computational refocusing algorithm described by Ng [13], but introduces a post-reconstruction filtering step that removes the blur caused by out of focus particles. The basis of this approach is that all light rays passing through a voxel containing a particle will have an irradiance value about some SNR threshold. In contrast, if a voxel does not contain a particle some or all of the light rays passing through it will have an irradiance value equivalent to zero. The post-reconstruction filter is applied by the following conditional. A voxel will only be assigned a non-zero intensity (via summation) if a minimum percentage (in theory 100%, typically 90-95%) of the light rays passing through that point have a recorded value above some minimum SNR threshold (chosen based on the raw image data). For voxels that contain light rays whose irradiance is zero, it is assumed that a particle cannot exist at this point and their intensity is set to zero. More information on this process can be found in Fahringer and Thurow [4].

In previous work [5], the reconstruction process used was an adaptation of tomographic reconstruction methods for use with plenoptic image data. Specifically, the multiplicative algebraic reconstruction technique (MART) introduced by Elsinga et al. [3] for tomo-PIV was implemented for plenoptic-PIV. These results showed that the MART algorithm was a viable method to reconstruct particle volumes from plenoptic image

data, however, the computational expense required, both in terms of the storage needed for the weighting matrix and the processing power needed to execute the iterative algorithm, was a limiting factor. As an example, if the data in this work was processed with MART, the weighting matrix would require 350 GB of disk space, and would take 5-8 hours to compute. Each image would then take an additional 20-30 minutes to process into a volume using a machine with 24 processing cores and 90 GB of RAM. In contrast, the filtered refocusing method does not require the computation of a weighting matrix and takes 6 minutes per image on the same machine. In addition, while this new algorithm is still in development, preliminary analysis in Fahringer and Thurow [4] indicates that the two methods have similar accuracy.

This process relies on the assumption that the individual microlens locations relative to the main lens optical axis are known. To ensure that this information is at hand, a microlens calibration is performed. In order to do this, the lens aperture must be set to be as small as possible, and a uniform planar target (e.g., illuminated card stock) must be placed at the object distance of the main lens, perpendicular to the optical axis. This results in a point image formed by every microlens. This image can be used to determine each microlens location [5].

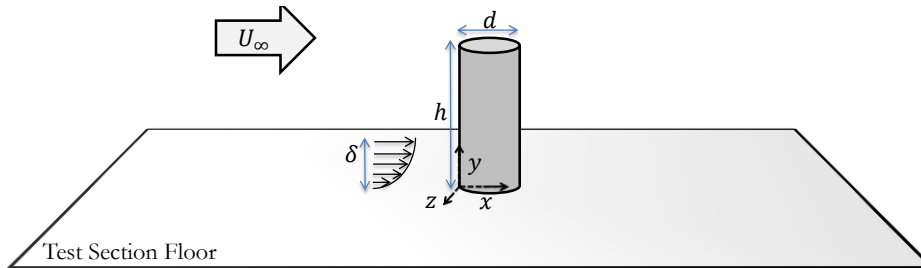


Fig. 5 Schematic of the cylinder model chosen for this work. The coordinate system is oriented at the leading edge of the cylinder's root. The freestream flow direction and abstraction of the boundary layer are shown. The cylinder diameter is  $d = 20$  mm and the aspect ratio is  $AR = h/d = 3$ .

### 3 Data Acquisition and Vector Calculation

The experimental flow platform used to test Plenoptic PIV compared to Tomographic PIV is the wake of a finite cylinder protruding from the boundary layer. SPIV data is provided as an auxiliary comparison. This experiment was selected because the flow field is well understood and contains rich three-dimensional structures. The scale of these structures are largely characterized by the Reynolds Number ( $Re_d$ ), the aspect ratio of the cylinder ( $AR = h/d$ ), and the boundary layer thickness ( $\delta/h$ ). The varying magnitude of these scales should test the dynamic range of both volumetric measurement methods.

The flow topology of the wake of a finite cylinder is well documented. In the work by Farivar, three main flow structures are identified: the arch vortex, the tip vortices, and the horseshoe vortex [6]. This and other works characterize the change in flow topology with respect to changing aspect ratio and flow conditions [6] [16] [19] [14] [17].

For all cases, the Reynolds number based on cylinder diameter is  $Re_d = 38,000$ . The cylinder aspect ratio is  $h/d = 3$  and the boundary layer height relative to the cylinder height is  $\delta/h = 0.45$ .

For all PIV measurement techniques in this study, particles are introduced to the flow, and a 200 mJ, double-pulse, Nd:YAG laser is used to illuminate the particles. Double-frame image pairs are captured, then the volumetric lightfield is reconstructed from the images (for the volumetric techniques). The cross-correlation of the image (volume) pairs is computed to determine the particle displacement within the flow.

#### 3.1 Stereoscopic PIV

Stereoscopic PIV (SPIV) is a well established method for generating three-component velocity data of flow within a planar region. Therefore, SPIV data can be considered a slice of the full volumetric data desired from Plenoptic or Tomographic PIV. This provides an additional measurement with which the Plenoptic PIV data can be compared.

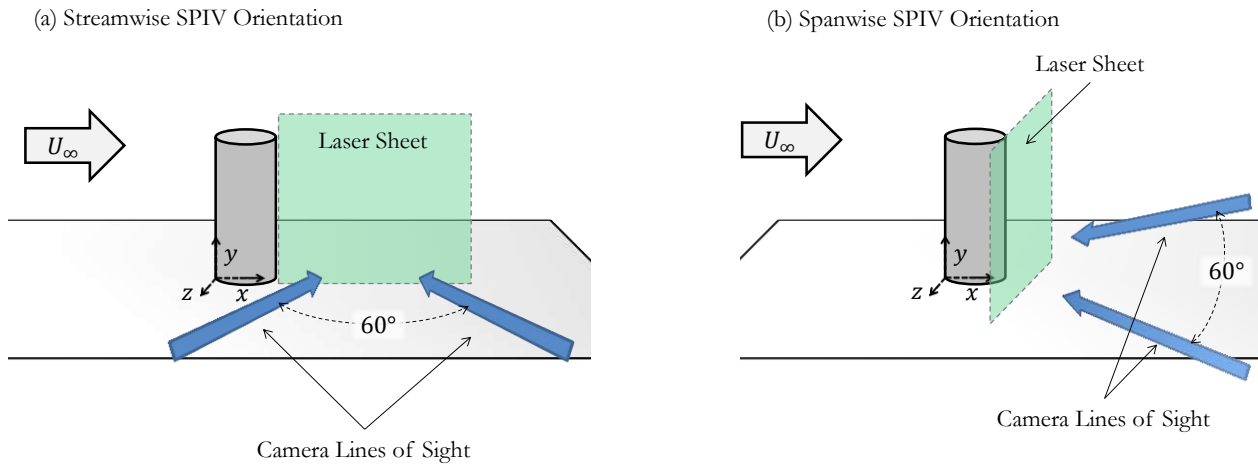


Fig. 6 (a) Schematic of the streamwise SPIV orientation. The laser sheet is aligned vertically with the  $x$ -axis. The line of sight for each camera is shown as blue arrows. For the streamwise orientation, the cameras image the flow from the same side of the cylinder. (b) Schematic of the spanwise SPIV orientation. The laser sheet is aligned vertically, parallel with the  $z$ -axis. The cameras are mounted on opposing sides of the test section.

In this section, details regarding the camera setup and the laser sheet orientation for the SPIV data are provided. Two laser orientations are used in this study - streamwise and spanwise. For the streamwise orientation, a laser sheet is generated in the wake of the cylinder and aligned vertically with the  $x$ -axis. Alternatively, for the spanwise orientation, the laser sheet is aligned vertically, parallel with the  $z$ -axis. Figure 6 illustrates both of these orientations.

The SPIV experiments are conducted in the Florida State Aeroacoustic Tunnel (FSAT). The FSAT is an open-return wind tunnel with a closed test section area of  $121.9 \text{ cm} \times 91.4 \text{ cm}$ . In both orientations, LaVision sCMOS 4 MP cameras are used with 180 mm lenses. Double frame images are acquired with a time separation of  $15 \mu\text{s}$ . Olive oil aerosol particles are introduced to the flow by a TSI 9307-6 oil droplet generator. The nominal size of the olive oil particles is  $1 \mu\text{m}$  [12]. The data acquisition, image processing, and vector calculation for the SPIV data is performed using LaVision DaVis ver. 8.2.x [9].

For the streamwise orientation, the cameras image the flow field from the side and have a relative angular offset of  $60^\circ$ . The laser light is focused by a spherical lens to a point near the measurement region in order to provide a beam waist of about 3 mm. A cylindrical lens is placed after the spherical lens in order to spread the light into a sheet. The laser illuminates the flow from underneath the test section.

In the spanwise configuration, the cameras are mounted on either side of the test section. The angular offset of the cameras is  $60^\circ$ . As in the streamwise orientation, a spherical and cylindrical lens is used to shape the light and the flow is illuminated from the side.

In both configurations, the laser and cameras are fixed to a traversing system in order to acquire several planes within the volume to be measured by Plenoptic and Tomographic PIV. For the streamwise case, the rig is traversed in the  $z$ -direction. For the spanwise case, the rig is traversed in the  $x$ -direction. 500 image pairs are acquired for every plane.

Some image processing is warranted before the vector calculation can be performed. In order to reduce reflections and other unwanted light from the images, the mean of the images is subtracted from the data set. Then, subsequent spatial Gaussian smoothing and sharpening is used to increase the clarity of the particle images.

For the vector calculation, the cross-correlation is calculated for iteratively smaller interrogation windows within the entire field of view. The beginning window size is  $96 \times 96$  pixels, and the final window size is  $64 \times 64$  pixels with 50% overlap. The final vector spacing is 2.7 mm per vector.

Each calculation of a vector field is followed by the correlation statistics uncertainty quantification method described by Wieneke [20]. This method derives the random uncertainty bounds by dewarping the second frame of each image pair based on the calculated cross-correlation. This should result in an identical image to the first frame. The differences between these images determine the random error in the vector calculation . A

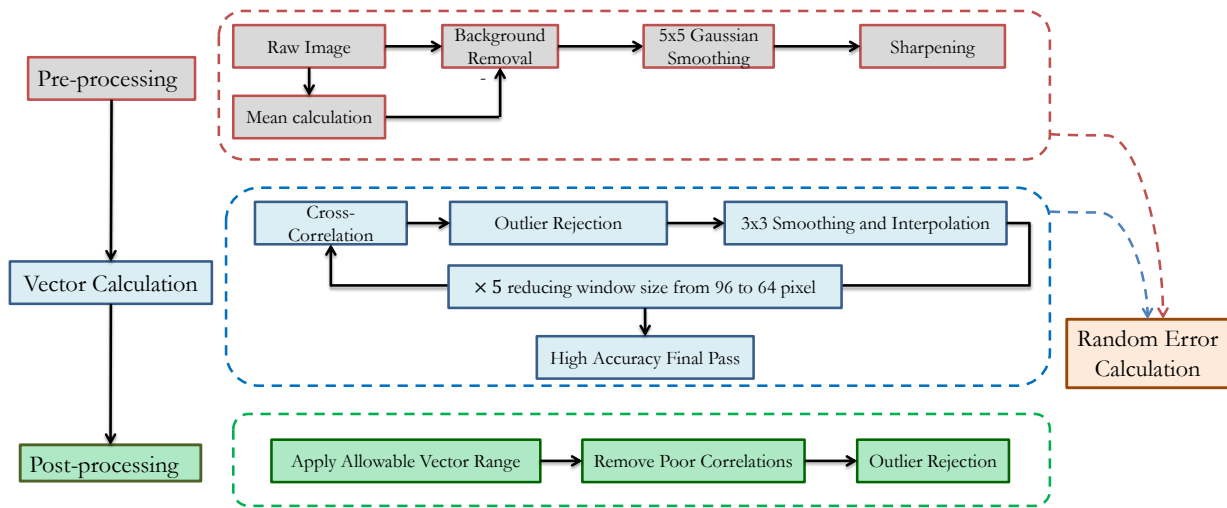


Fig. 7 Chart of the processing steps taken for SPIV vector calculation.

detailed flow chart of the processing steps is provided in Figure 7.

### 3.2 Tomographic PIV

The Tomographic PIV experiment is conducted in the FSAT facility, similar to the SPIV case. A four camera configuration is used to acquire the images for Tomographic PIV. The camera system consists of two sCMOS LaVision cameras and two CCD Imager ProX LaVision cameras. All four cameras are viewing the flow from the same side. The angular offset of each camera is nominally 30° as recommended by [3]. Olive oil particles are used as seed similar to the SPIV run. The seed particles are illuminated from under the test section. Two cylindrical lenses are used to shape the light into an elliptical cross-section. A rectangular aperture is used to further refine the volume of light into a rectangular cross-section. A schematic of the Tomographic PIV setup is shown in Figure 8.

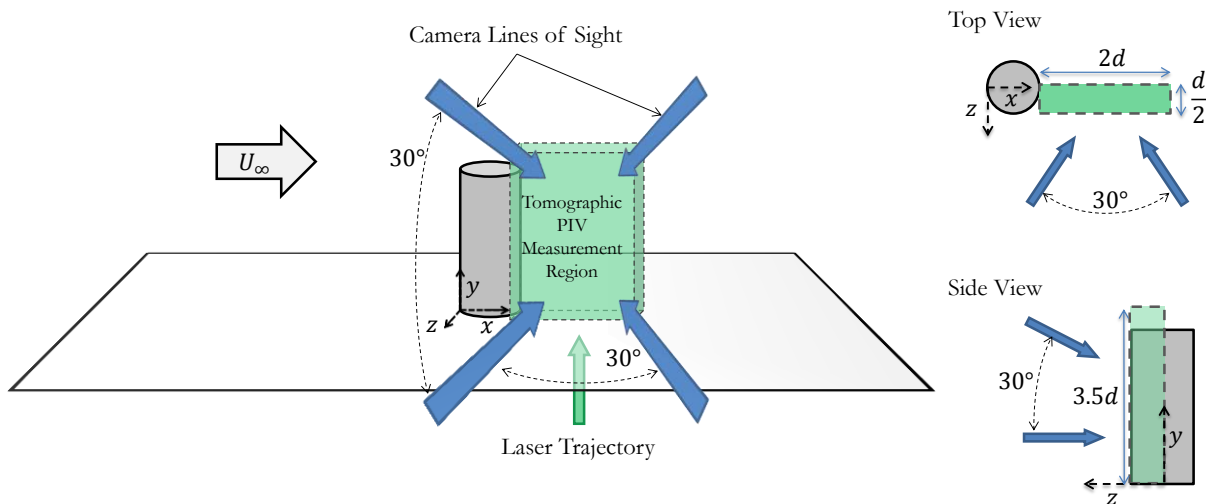


Fig. 8 Schematic of the Tomographic PIV system. The approximate dimensions of the measurement volume is given. The line of sight for each camera is shown as blue arrows.

The ProX CCD cameras have a lower bit-depth than the sCMOS cameras, so the CCD cameras are mounted higher than the sCMOS cameras in order to take advantage of the increased forward scatter from the laser. 105 mm lenses are used for the closer sCMOS cameras, and 180 mm lenses are used for the CCD cameras. 500 image pairs are acquired for each camera. The data acquisition, image processing, volume reconstruction, and

vector calculation for the Tomographic PIV experiment are performed using LaVision DaVis ver. 8.2.x [9].

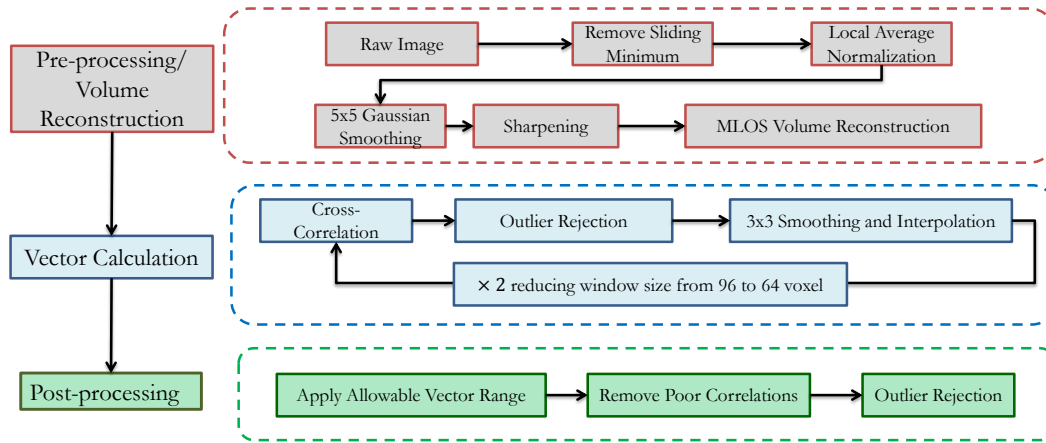


Fig. 9 Chart of the processing steps taken for Tomographic PIV vector calculation.

The image processing steps for this data differs somewhat from the steps for the SPIV data. To begin, a sliding minimum subtraction and an intensity normalization are performed to reduce the background illumination and correct for non-uniform illumination. Then, Gaussian smoothing and sharpening filters are applied sequentially. The Multiplicative Line of Sight (MLOS) method is employed to reconstruct the illuminated volume from the images. The MLOS algorithm is chosen due to the reduced computational time for volume reconstruction compared to the MART algorithm. In future studies, performing the volume reconstruction with the MART algorithm may be warranted. The dimension of the reconstructed volume is  $2.5d \times 4d \times 0.7d$  with  $1385 \times 2216 \times 388$  voxels.

The volumetric cross-correlation is performed on iteratively smaller interrogation regions. The final interrogation region dimensions are  $64 \times 64 \times 64$  voxels. 75% overlap is used on the final pass, so the final vector resolution is  $\Delta x_i = 0.58$  mm per vector. Figure 9 contains a flowchart of the Tomographic PIV processing steps.

### 3.3 Plenoptic PIV

The Plenoptic PIV experiment is performed in the Florida State Advanced Technology for Aeronautics Demonstrator (FATAD) wind tunnel. The FATAD is a open-return wind tunnel with test section area of  $30.5 \text{ cm} \times 30.5 \text{ cm}$ . Care was taken when designing the experimental setup for the Plenoptic PIV acquisition. It has been shown in prior literature [5] that reconstructed particles exhibit a significant elongation in the direction of the main lens optical axis. As such, it is hypothesized that the dynamic range of the vector calculation is reduced in this direction. Therefore, the camera should be oriented such that the most interesting velocity components are normal to the optical axis. For this experiment, the most interesting components are the  $u$  and  $w$  velocity components. Therefore, it was decided that the plenoptic camera be oriented parallel to the  $y$ -axis, in order to capture the  $v$ -component of velocity.

The flow is seeded with DEHS particles, in which the nominal particle diameter is around  $1 \mu\text{m}$ . Illumination is introduced from the side of the test section. To provide sufficient light for clear particle images, the laser volume cross-section is limited to around  $1.2 d^2$  and the light passes through the test section a second time due to a mirror fixed to the opposing test section wall.

Plenoptic images of the flow are acquired by a modified Imperx ICL-B6620W camera with a Kodak KAI-29050 photosensor. The microlens array consists of hexagonally arranged microlenses with a pitch of 77 microns and focal length of 308 micron. A total of  $471 \times 362$  microlenses populate the array. Double frame images are captured with a separation of  $\Delta t = 30 \mu\text{s}$ .

Since the camera is oriented parallel to the  $y$ -axis, a portion of the volume measured by Tomographic PIV would be lost. In order to span the entire region captured by Tomographic PIV, several volumes are captured by Plenoptic PIV with the intent to stitch the statistical results together a posteriori. Very little effort is required to accomplish this, since Plenoptic PIV requires only one camera for full volumetric measurements. The plenoptic

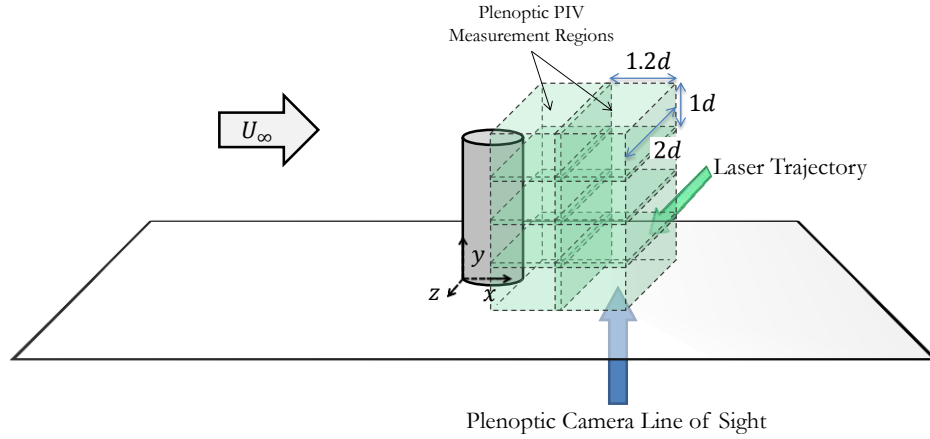


Fig. 10 Schematic of the Plenoptic PIV setup. The approximate dimensions of the measurement volumes is given. 8 volumes are measured. The line of sight for the camera is shown as a blue arrow.

camera was mounted to a precision micro-traverse, and was translated accordingly. This illustrates a practical asset of Plenoptic PIV.

Figure 10 provides details regarding the dimension and orientation of the volumes measured by Plenoptic PIV. A total of 300 image pairs are acquired for each volume. After the data is acquired, a microlens calibration image is taken to be used for volume reconstruction.

Processing the plenoptic images provided a unique set of challenges. Specifically, spatial filters should not be applied to the raw plenoptic images since the length scale of the filters is on the order of the microlens image size. This can result in altered microlens images, which will detrimentally affect the volume reconstruction. Additionally, it was found that temporal mean or minimum subtraction removed contribution from particles that are some distance from the object plane. So no image processing is performed on the raw plenoptic images.

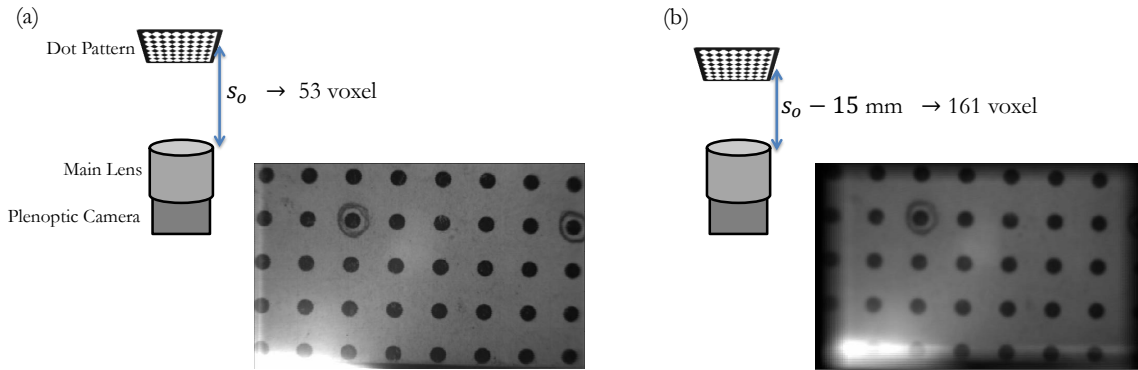


Fig. 11 Slices of the calibration pattern volume reconstruction for the calibration plate oriented at (a) the object distance of the main lens and (b) 15 mm closer to the lens. The dark edges on (b) indicate the trapezoidal shape of the reconstructed volume. This is due to the increase in magnification for objects closer to the lens. Each slice of the volume is interpolated to the same grid to ensure a constant voxel scaling.

The volume reconstruction is performed as described in section 2. The dimensions of the reconstruction volume as well as the number of voxels per dimension need to be defined. These parameters are chosen in order to reconstruct a physically significant portion of the volume measured while balancing the computational cost and time required to reconstruct such a volume. As such, the reconstructed volume is a truncated version of the entire volume measured. The number of voxels are  $260 \times 180 \times 420$  in the  $x$ ,  $y$ , and  $z$  directions. In this case, the reconstructed volume size is optimized for reduced computational time while providing sufficient resolution for a preliminary analysis. This results in a spatially undersampled volume and future work will incorporate volume reconstructions that are optimized for vector resolution.

The volume reconstruction results in a three-dimensional uniformly spaced array of voxel brightness levels corresponding to the source of the plenoptic image. In order to determine the scaling estimate, a volume spatial calibration is performed.

In this case, 5 images of a well defined planar dot-pattern are acquired by the plenoptic camera. For the first image, the dot pattern was placed at the object distance of the main lens. For each successive image, the dot-pattern is traversed toward the camera by 5 mm. The volume reconstruction is performed on each of these images to determine the appropriate voxel spacing in the  $x$ ,  $y$ , and  $z$  directions. Figure 11 contains two volume slices of this dot pattern. One slice is at the object distance of the main lens, the other is 5 mm closer to the camera.

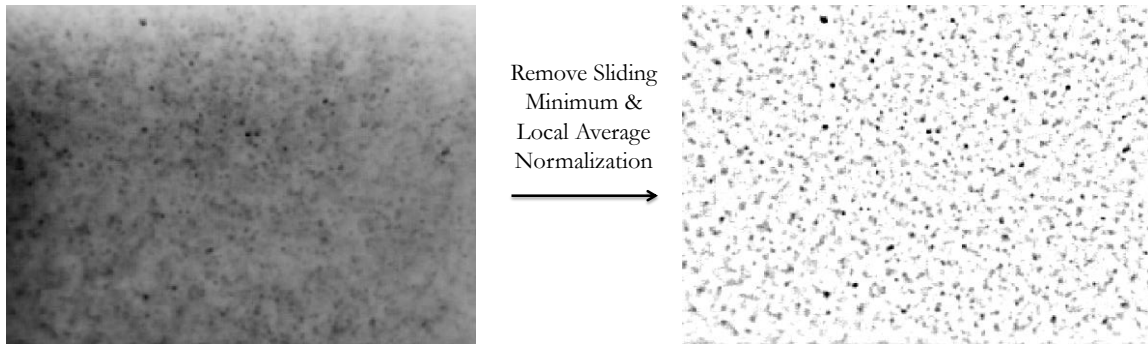


Fig. 12 Inverted plenoptic particle volume slice illustrating the sliding minimum removal and local average normalization steps for correcting the non-uniform illumination.

Two aspects of the plenoptic volume scaling can be gleaned From Figure 11. First, the edges of the dot pattern volume slice closer to the camera are lost. This illustrates the fact that the shape of the volume sampled is a trapezoidal prism. This is due to the angle of view of the main lens. Second, the voxel scaling can be determined based on the dot pattern spacing. The scaling within the plane of the dot card is  $\Delta x = \Delta z = 0.086$  mm per voxel. In determining the voxel spacing in the  $y$ -direction, the  $y$ -voxel location of the reconstructed view of the dot card is determined after the dot card is shifted in the  $y$ -direction by 5 mm. Shifting the dot pattern 5 mm closer to the camera results in a voxel shift of 36. This provides an accurate measure of the voxel scaling in the axial direction. The voxel size in this direction is 0.139 mm per voxel. From these results, the size of each reconstructed volume is  $1.1d \times 1.25d \times 1.8d$ .

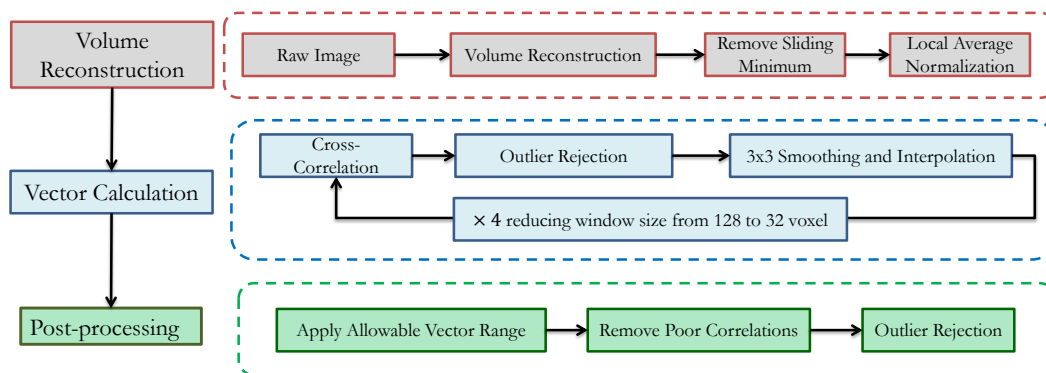


Fig. 13 Chart of the processing steps taken for Plenoptic PIV vector calculation.

Once the volumes are reconstructed, spatial filters are applied to reduce out-of-focus light and to correct for non-uniform illumination. For every slice of the volume, a 2-D sliding minimum removal and local average normalization is performed. The result of this process is shown for an arbitrary slice of a reconstructed volume in Figure 12.

At this point, the reconstructed volumes are imported into DaVis for vector calculation. A multi-pass

approach is taken with iteratively smaller interrogation regions. The scale of the initial interrogation region is 128 voxel and the scale of the final interrogation region is 32 voxel. With an overlap of 75% the final average vector resolution is  $\Delta x = 0.69$ ,  $\Delta y = 1.11$ ,  $\Delta z = 0.69$  mm per vector. Figure 13 contains a flow chart of the processing steps taken for Plenoptic PIV.

In the sections that follow, a comparison of the data acquired by Plenoptic PIV and Tomographic PIV will be compared using the SPIV results as a metric.

## 4 Results

### 4.1 Mean Flow

The mean velocity fields are computed from the Plenoptic and Tomographic PIV measurements. These data are stationary, so the mean should converge provided that a sufficient number of samples exist. A convergence analysis is performed to illustrate the point in which sufficient samples are used in the mean calculation.

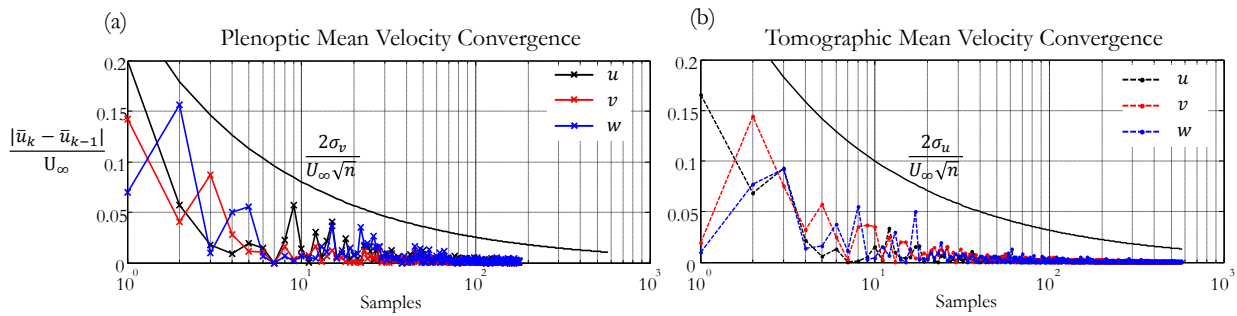


Fig. 14 Plots of the difference between mean values using  $k$  samples and  $k - 1$  samples for a single data point from (a) Plenoptic PIV measurements and (b) Tomographic PIV measurements. The data point is defined as the closest grid point to  $x/d = 2.85$ ,  $y/d = 1.81$ , and  $z/d = -0.1$ . This point is indicated in Figure 16. These plots show that the mean converges to within a difference of 0.3% of  $U_\infty$  after 100 samples for both measurement methods. The convergence envelope based on 95% reliability margin as described in [1] is shown as the solid black line.

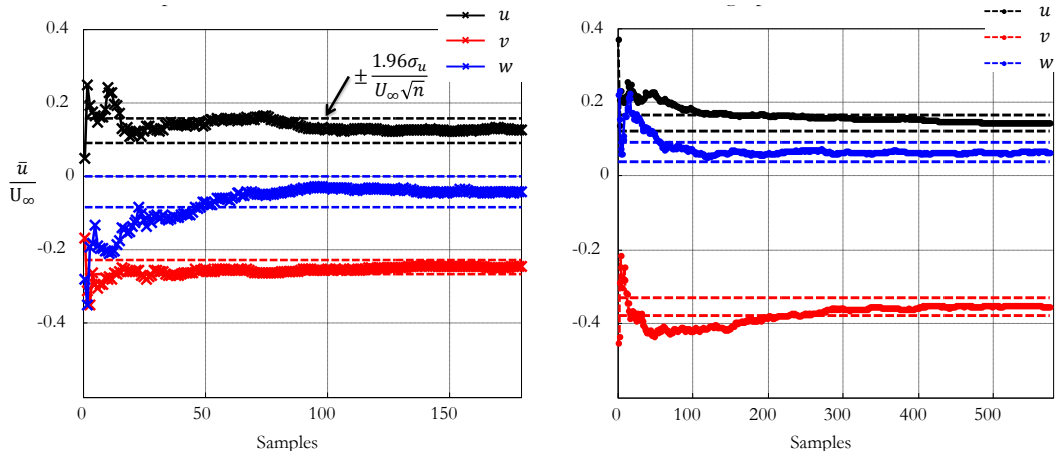


Fig. 15 Plots of the running mean calculated for increasing samples from (a) Plenoptic PIV measurements and (b) Tomographic PIV measurements. The data point is defined as the closest grid point to  $x/d = 2.85$ ,  $y/d = 1.81$ , and  $z/d = -0.1$ . This point is indicated in Figure 16. 95% confidence intervals are provided as horizontal dashed lines for each velocity component. The fact that these envelopes do not overlap indicate that some bias exists in the mean calculated between the measurement methods.

For this convergence analysis, the mean is calculated from  $k$  samples of Plenoptic and Tomographic PIV measurements. This process is repeated with an additional sample included per iteration. For a converged mean

value, the difference between the current and prior mean calculation will be zero. So, the difference in the mean is calculated between the current and prior iterations, and a plot of this is shown for an arbitrary point within the measurement grid in Figure 14. For this study, a difference of less than 0.3% of the freestream velocity will imply convergence. The result of this analysis is that at least 100 samples are required to meet the mean convergence criterion for Plenoptic PIV. The running mean calculation for increasing samples is shown for this point in Figure 15. The conventional 95% confidence intervals are shown as dashed horizontal lines for each velocity component. The fact that these bounds do not match between the plenoptic and tomographic results indicate that some bias exists between the measurement methods.

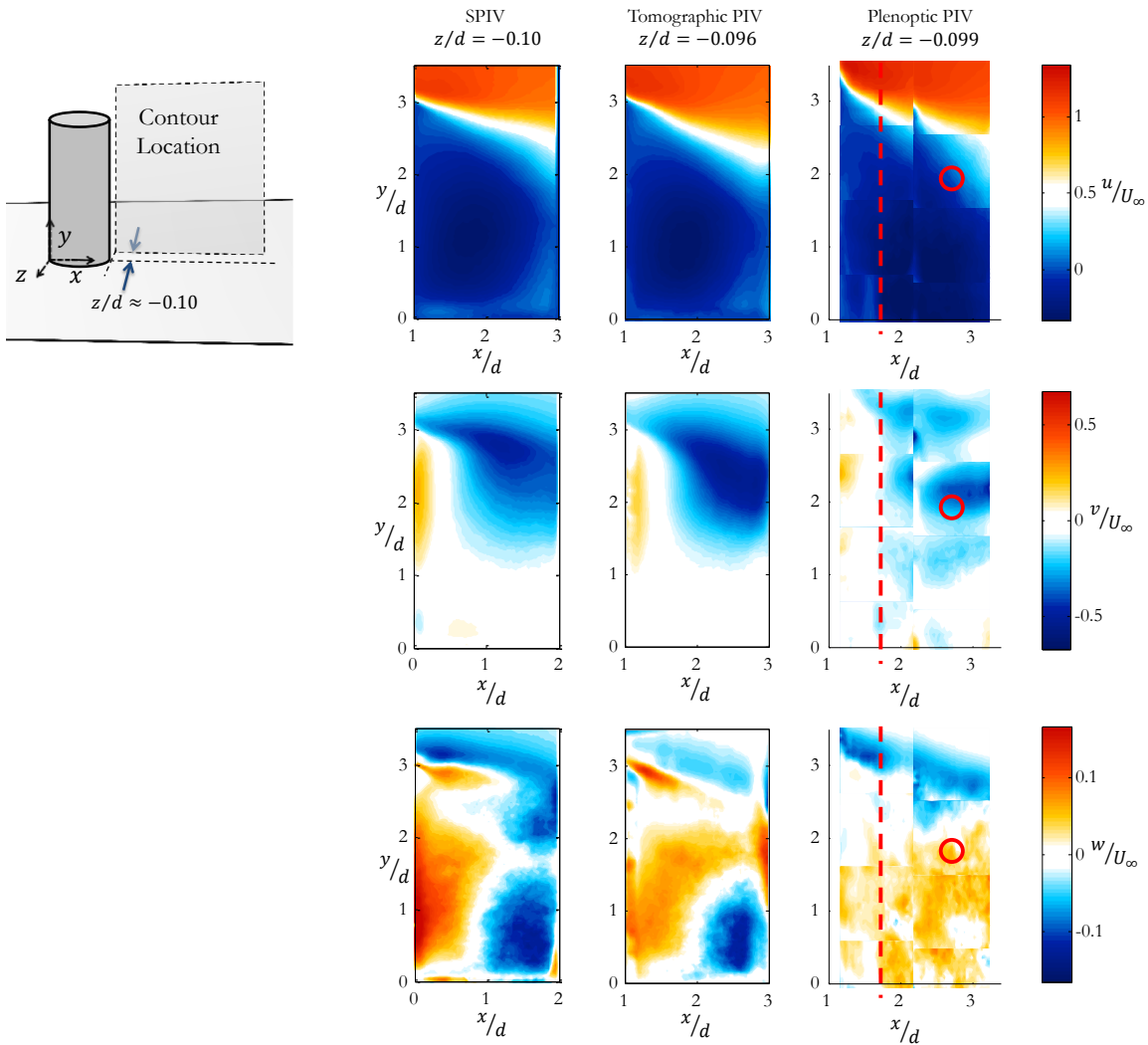


Fig. 16 Mean velocity contours along a streamwise plane of the measurement region. 500 snapshots are used for the SPIV and Tomographic PIV mean calculation. 180 snapshots are used for the Plenoptic PIV mean calculation. The spanwise location of the contours correspond to the closest grid location to  $z/d = -0.10$ . Note the similarities between all measurement methods for the  $u$  and  $w$  velocity components. Slight disparities can be attributed to differences in spanwise location due to measurement grid discretization. There are also apparent issues in patching together the plenoptic volumes. This is partly caused by the difference in the number of samples used for the mean calculation. Since a significant velocity gradient exists at the edge of the reconstructed volumes, any deficiencies in mean convergence will be exaggerated at the edges. The  $v$  velocity component as measured by Plenoptic PIV exhibits some clear differences compared to SPIV and Tomographic PIV. Since the  $y$  axis is parallel to the plenoptic camera optical axis, particle stretching occurs in this direction. This results in a decrease in the velocity dynamic range in this direction. The red line indicates the location of the velocity profiles provided in Figure 17. The red circle indicates the spatial point used for the mean convergence analysis.

With convergence verified, 500 snapshots are used to compute the mean velocities for the SPIV and Tomographic PIV experiments. Due to the substantial time required for reconstructing the volumes for Plenoptic PIV, significantly less samples are currently available. For each volume measured by Plenoptic PIV, 180 snapshots are used to compute the mean. Although less samples are available for Plenoptic PIV, the mean convergence criterion is still met.

Figure 16 provides mean velocity contours for the  $u$ ,  $v$ , and  $w$  velocity components from the SPIV, Tomographic PIV, and Plenoptic PIV measurements. These contours correspond to a slice of the total volumes recorded by Tomographic and Plenoptic PIV. Since each measurement grid differs between the measurement method, the location of the contour plotted will vary slightly. Therefore, minor deviations in the contour levels are expected between the three measurement methods. Also, some inconsistencies exist at the seams of the plenoptic volumes due to inevitable experimental imperfections, the suboptimal voxel resolution, and possible errors in the plenoptic calibration parameters. These concerns are all topics of current and future work in the development of Plenoptic PIV. Given these facts, note the similarities between all measurement methods for the  $u$  and  $w$  velocity components. However, the  $v$  velocity component as measured by Plenoptic PIV exhibits some clear differences compared to SPIV and Tomographic PIV. This is due in part by an insufficient convergence criterion. Since a significant velocity gradient exists at the edge of the reconstructed volumes, any deficiencies in mean convergence will be exaggerated at the edges. Therefore, this will improve with additional samples used for the mean calculation. Additionally, since the  $y$  axis is parallel to the plenoptic camera optical axis, particle stretching occurs in this direction. This results in a decrease in the velocity dynamic range in this direction. Reprocessing this data with optimized volume reconstruction parameters will improve the performance in this direction.

In Figure 17 the mean flow profiles for the  $x$ ,  $y$ , and  $z$  components are shown. The profile locations correspond to the closest PIV grid point to  $x/d = 1.8$  and  $z/d = 0.1$ . The Stereo PIV results are plotted with uncertainty levels in the shaded region.

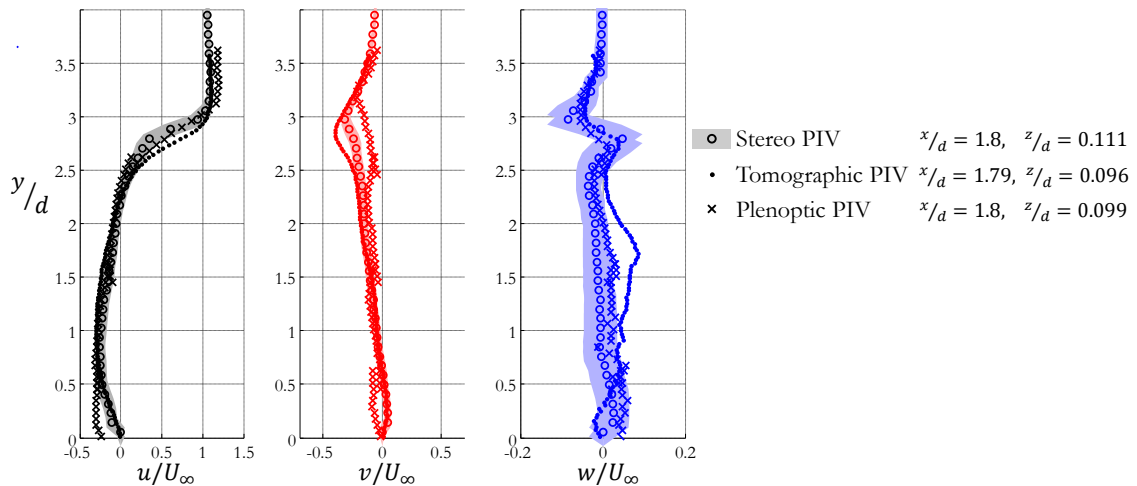


Fig. 17 Velocity profiles as measured with SPIV, Tomographic PIV and Plenoptic PIV.  $x/d \approx 2$  and  $z/d \approx 0.1$ . The location of the profile is indicated by the red dashed line in Figure 16. The SPIV data are shown as circles, with shaded uncertainty bounds. The Tomographic PIV data are shown as dots. The Plenoptic PIV results are shown as crosses. 500 snapshots are used to compute the mean for the SPIV and Tomographic PIV profiles, while 180 snapshots are used in the Plenoptic PIV mean. The Plenoptic PIV data matches well with the SPIV results for the  $u$  and  $w$  components, with some disparity in the  $v$  component. This can be attributed to the slight difference in the relative location of the profile and the fact that significantly less snapshots are used for the Plenoptic PIV mean calculation. The Tomographic PIV results exhibit some differences with respect to the SPIV data for the  $w$ -velocity component.

## 4.2 Statistics

A convergence analysis with respect to the Reynolds stress components is performed in a similar fashion to the mean convergence analysis mentioned prior. A plot of the normalized difference of the Reynolds stress components for increasing number of snapshots is shown in Figure 18. For all Reynolds stress components, the normalized difference converges to within  $3 \times 10^{-3}$  for over 100 snapshots. For this analysis, this condition will serve as the convergence criterion for the Reynolds stress components.

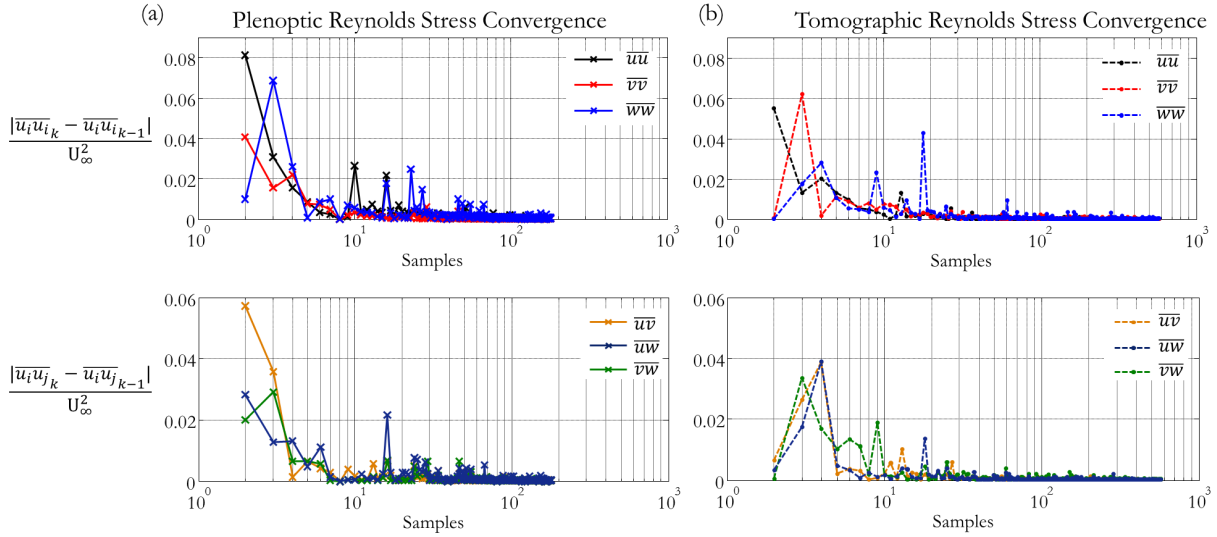


Fig. 18 Plots of the difference between the Reynolds stress components using  $k$  samples and  $k - 1$  samples for a single data point of (a) Plenoptic PIV measurements and (b) Tomographic PIV measurements. The data point is defined as the closest grid point to  $x/d = 2.85$ ,  $y/d = 1.81$ , and  $z/d = -0.1$ . These plots shows that the Reynolds stress components converge to within a normalized difference of  $3 \times 10^{-3}$  with 100 snapshots. This is taken to be the convergence criterion for the Reynolds stress components.

The calculated Reynolds stress tensor components for increasing number of samples is provided in Figure 19. The 95% confidence interval has been calculated for the Reynolds stress components as in Benedict and Gould [2]. This interval is shown for each Reynolds stress component as dashed horizontal lines. These regions do not overlap for all Reynolds stress components which verify that a bias error exists between the tomographic and plenoptic Reynolds stress component estimates.

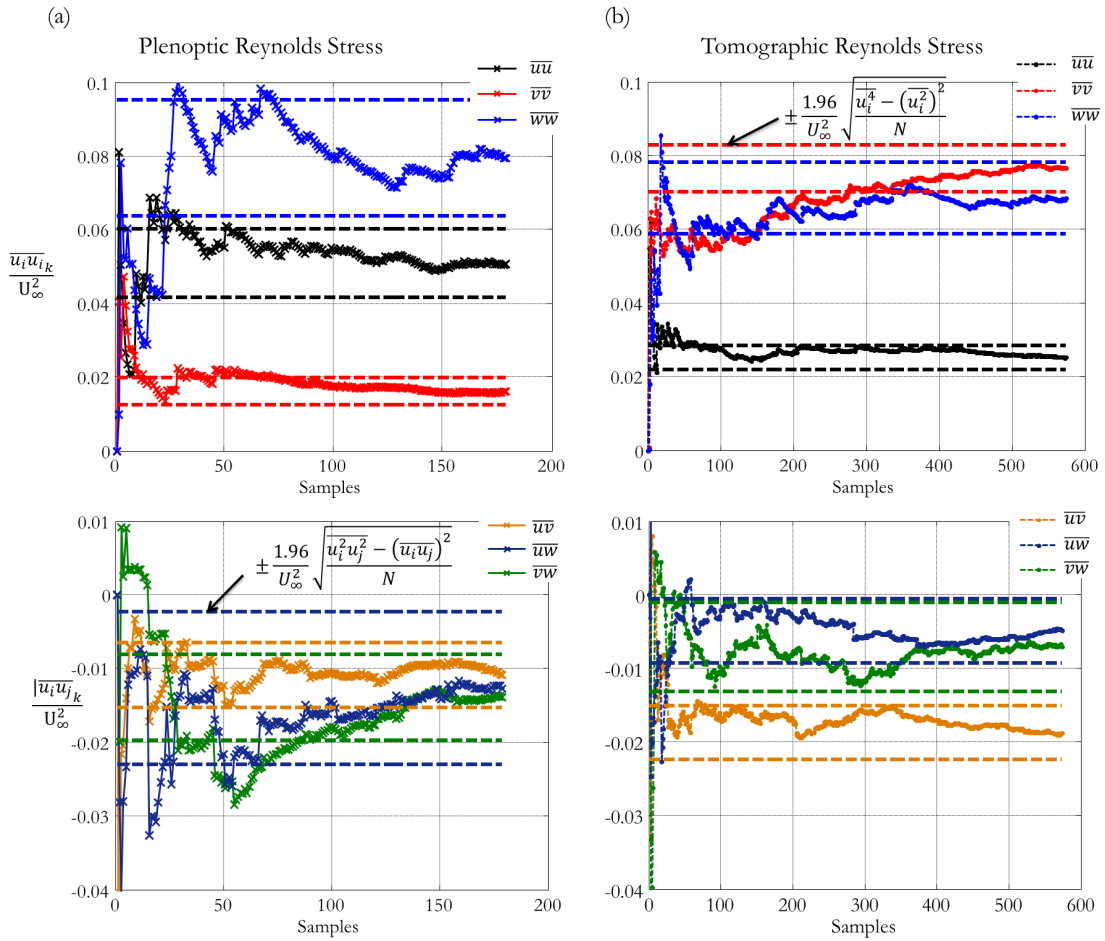


Fig. 19 Plots of the Reynolds stress components calculated for increasing samples from (a) Plenoptic PIV measurements and (b) Tomographic PIV measurements. The data point is defined as the closest grid point to  $x/d = 2.85$ ,  $y/d = 1.81$ , and  $z/d = -0.1$ . This point is indicated in Figure 20. 95% confidence intervals are provided as horizontal dashed lines for each velocity component. The expression used to calculate the confidence interval is shown on the plot, and can be found in Benedict and Gould [2]. The fact that many of these envelopes do not overlap indicate that some bias exists in the Reynolds stress estimates between the measurement methods.

Figure 20 shows contour plots of the diagonal Reynolds stress tensor components as computed from SPIV, Tomographic PIV, and Plenoptic PIV measurements. Some features are shared between the three measurement methods, however significant differences are seen for the Plenoptic PIV  $\overline{v v}$  component. From the figure, large deviations from the mean are concentrated about the region of the highest downwash. And, surrounding this region, an underprediction of the deviations exist in regions of low  $v$ -velocity. This apparent banding is due to the decreased dynamic range of the Plenoptic PIV measurements in the  $y$ -direction. This effect is more apparent in this case as opposed to the mean velocities since these are squared values. The off-diagonal Reynolds stress tensor components are shown in Figure 21.

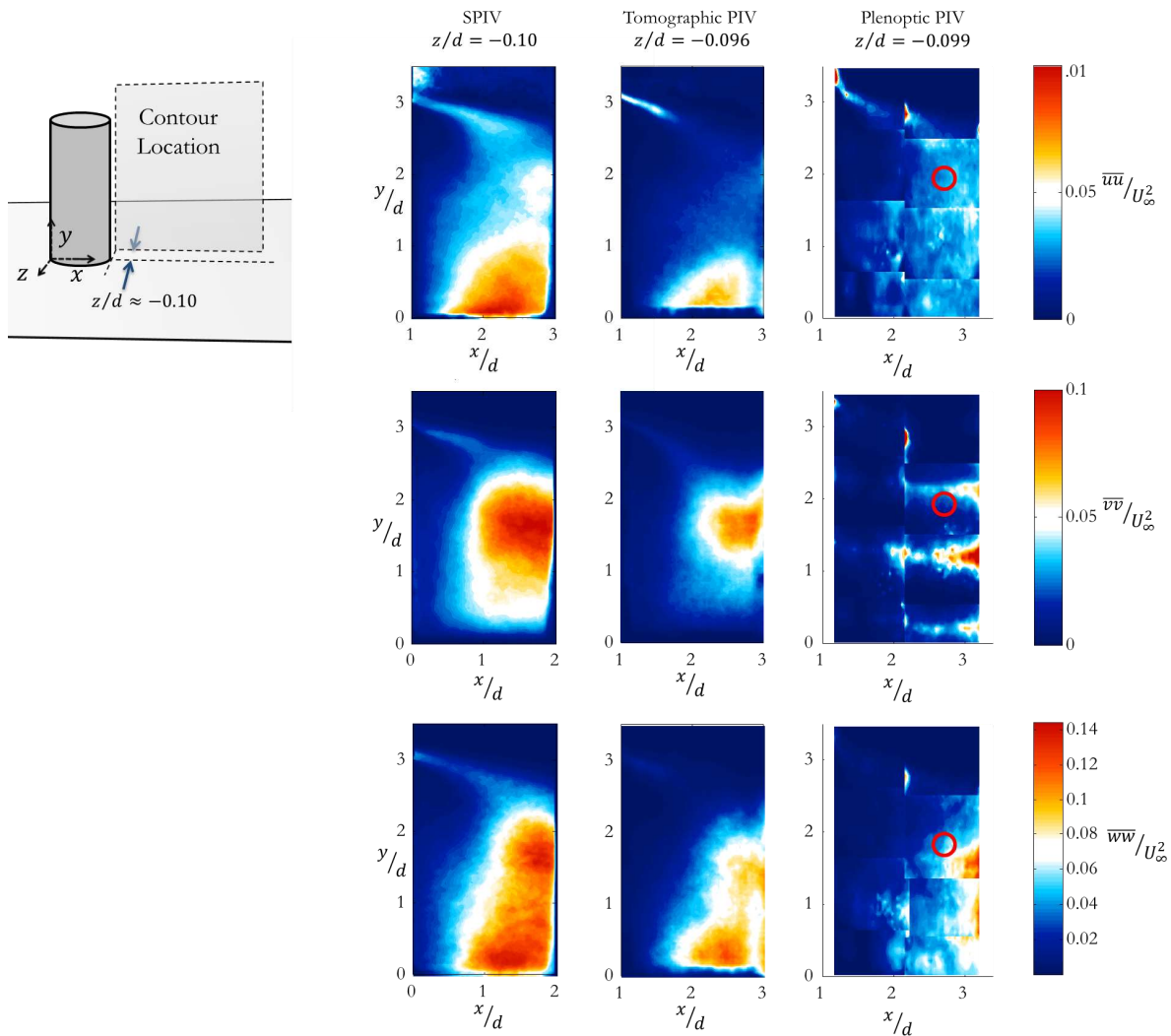


Fig. 20 Diagonal Reynolds stress component contours along a streamwise plane of the measurement region. 500 snapshots are used for the SIV and Tomographic PIV Reynolds stress calculation. 180 snapshots are used for the Plenoptic PIV Reynolds stress calculation. The spanwise location of the contours correspond to the closest grid location to  $z/d = -0.10$ . The Plenoptic PIV  $\bar{v}'v'$  component suffers from the perceived particle elongation in the  $y$ -direction. This effect is exaggerated for the Reynolds stress estimates since these are squared quantities. The red circle indicates the point taken for the Reynolds stress convergence analysis.

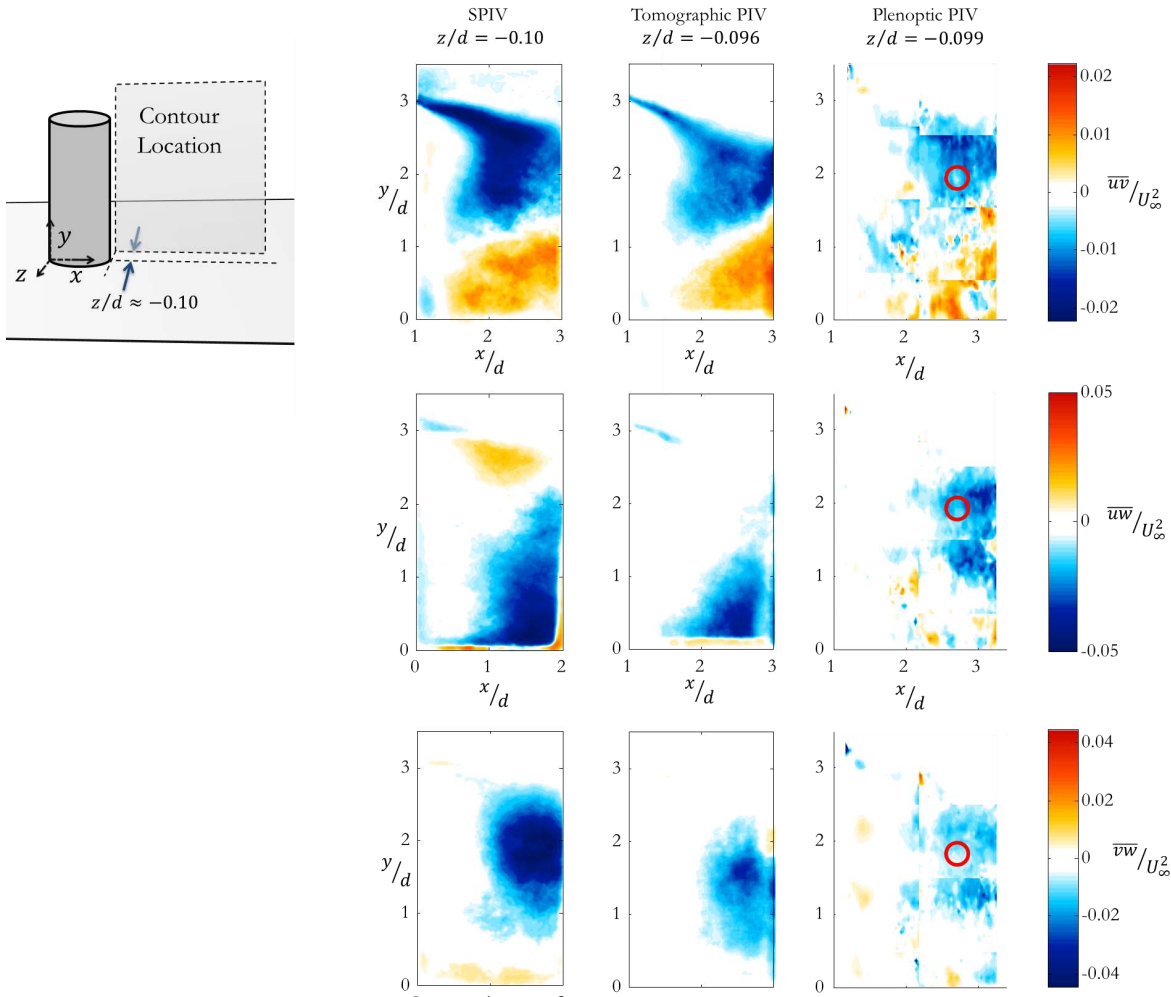


Fig. 21 Off-diagonal Reynolds stress component contours along a streamwise plane of the measurement region. 500 snapshots are used for the SPIV and Tomographic PIV Reynolds stress calculation. 180 snapshots are used for the Plenoptic PIV Reynolds stress calculation. The spanwise location of the contours correspond to the closest grid location to  $z/d = -0.10$ . The red circle indicates the point taken for the Reynolds stress convergence analysis.

## 5 Conclusion

For both methods, a volumetric portion of the wake of a cylinder protruding from a boundary layer is measured. The size of the volumes measured by Tomographic and Plenoptic PIV are comparable with the latter being somewhat larger. However - due to the orientation of the measurement volume, several Plenoptic PIV volumes are required in order to span the entire region measured by Tomographic PIV. The ability to easily traverse the single plenoptic camera for multiple volumetric flow acquisitions is a benefit of Plenoptic PIV that was utilized for this study.

The new Filtered Refocusing (FR) reconstruction method is employed to reconstruct the volumetric particle field imaged by the plenoptic camera. Once this is performed, a volumetric spatial calibration is applied to account for optical refraction due to the acrylic walls of the test section. Finally, conventional PIV image processing and 3-D cross-correlation is used to generate the volumetric vector field.

In comparing the mean of Tomographic and Plenoptic PIV measurements of the wake of a cylinder protruding from a boundary layer, both methods provide similar results. Some discontinuities appear near the edges when stitching the plenoptic measurement volumes together to visualize the mean flow. This is partly due to the plenoptic volume discretization being sub-optimal, uncontrollable experimental parameters, and the number of samples used in the mean calculation. Additionally, both tomographic and plenoptic methods exhibit

relatively weak agreement in one velocity component with respect to the SPIV measurements. For Plenoptic PIV, this weak agreement is seen in the  $v$ -velocity component. This is the component that is aligned with the optical axis of the plenoptic camera. It has been shown that the plenoptic particle reconstructions are elongated in this direction. Therefore, additional error in this component is expected. For Tomographic PIV, the weak velocity component is the  $w$ -velocity. This component corresponds to the axis about which all four cameras are centered. Therefore, if the relative angle is increased between the cameras, the error should decrease. However, increasing the angle between the cameras increases the burden of optical access for the experiment.

The effect of the particle elongation is exacerbated in the Reynolds stress analysis. However, this can be eased by properly designing the experiment such that the plenoptic camera's line of sight is oriented with the velocity component that is of the least importance. Also, optimizing the volume reconstruction parameters will improve the performance in this direction. Additional work is warranted in addressing this aspect of plenoptic particle reconstruction.

In summary, the results provided demonstrate the potential for Plenoptic PIV to be adopted as a viable volumetric measurement method for many 3-D flows of interest. Additionally, Plenoptic PIV allows for volumetric fluid velocity data to be acquired in facilities that were once inhibited by limited optical access. With respect to the well established, commercially available Tomographic PIV measurement methods; and considering the fact that Plenoptic PIV is still in its early stages of development, the results provided by Plenoptic PIV compare favorably to Tomographic PIV measurements. In addressing the practical concerns highlighted in this work, Plenoptic PIV will continue to mature.

## References

- [1] Adrian, R., Westerweel, J. (2011). *Particle Image Velocimetry* (Vol. 30). Cambridge University Press.
- [2] Benedict, L., Gould, R., (1996) *Towards better uncertainty estimates for turbulence statistics* . Experiments in Fluids 22, pp 129-136.
- [3] Elsinga, G. E., Scarano, F., Wieneke, B., van Oudheusden, B. W., (2006), *Tomographic particle image velocimetry* , Exp Fluids 41:933-947.
- [4] Fahringer, T., and Thurow, B., (2015) *Comparing volumetric reconstruction algorithms for plenoptic PIV*, AIAA Paper 2015-1221, 53rd AIAA Aerospace Sciences Meeting, Kissimmee, Florida, January 4-8, 2015.
- [5] Fahringer, T. W., Thurow, B. S., (2012), *Tomographic Reconstruction of a 3-D Flow Field Using a Plenoptic Camera* , 42nd AIAA Fluid Dynamics Conference and Exhibit, New Orleans, Louisiana.
- [6] Farivar, D., (1981) *Turbulent Uniform Flow around Cylinders of Finite Length* , AIAA Journal, Vol. 19, No. 3 (1981), pp. 275-281.
- [7] Hecht, E., (2002), *Optics* , Addison-Wesley.
- [8] Georgiev, T., Intwala, C., (2006), *Light field camera design for integral view photography* ., Adobe System, Inc.
- [9] DaVis v8.2 (2014), LaVision, Software Package.
- [10] Levoy, M., Hanrahan, P., (1996), *Light Field Rendering* , SIG-GRAPH 96, 31-42.
- [11] Lynch, K., Fahringer, T., Thurow, B., (2012), *Three-Dimensional Particle Image Velocimetry Using a Plenoptic Camera* , 50th AIAA Aerospace Sciences Meeting including the New Horizons Forum and Aerospace Exposition, Nashville, Tennessee.
- [12] Melling, A., (1997) *Tracer particles and seeding for particle image velocimetry*, Meas. Sci. Technol. 8, 1406-1416.
- [13] Ng, R., Levoy, M., Bredif, M., Duval, G., Horowitz, M., Hanrahan, P., (2005), *Light Field Photography with a Hand-held Plenoptic Camera* , Standford Tech Report CTSR 2005-02.
- [14] Okamoto, T., Yagita, M. (1973). *The experimental investigation on the flow past a circular cylinder of finite length placed normal to the plane surface in a uniform stream*. Bulletin of JSME, 16(95), 805-814.

- [15] Pattenden, R., ((2005), *Measurement of the Flow Over a Low Aspect Ratio Cylinder Mounted on a Ground Plane*, Experiments in Fluids 39, pp. 10-21
- [16] Rostamy, N., (2013), *Instantaneous Flow Field Above the Free End of Finite-Height Cylinders and Prisms*, International Journal of Heat and Fluid Flow, Vol. 43, pp. 120-128
- [17] Sakamoto, H., (1983), *Vortex Shedding from a Rectangular Prism and a Circular Cylinder Placed Vertically in a Turbulent Boundary Layer*, Journal of Fluid Mechanics, 126, pp. 147-165
- [18] Scarano, F., (2013) *Tomographic PIV: principles and practice*, Meas. Sci. Technol. 24(1), 012001.
- [19] Sumner, D., (2004), *Wake Structure of a Finite Circular Cylinder of Small Aspect Ratio*, Exp Fluids 37, pp. 720-730.
- [20] Wieneke, B., (2014), *Generic a-posteriori Uncertainty Quantification for PIV Vector Fields by Correlation Statistics*, 17th International Symposium on Applications of Laser Techniques to Fluid Mechanics, Lisbon, Portugal.